Comparison of CIGS Solar Cells Made With Different Structures and Fabrication Techniques

Lorelle M. Mansfield, Rebekah L. Garris, Kahl D. Counts, James R. Sites, Christopher P. Thompson, William N. Shafarman, and Kannan Ramanathan

***Abstract*—Cu(In, Ga)Se_2 (CIGS)-based solar cells from six fabricators were characterized and compared. The devices had differing substrates, absorber deposition processes, buffer materials, and contact materials. The effective bandgaps of devices varied from 1.05 to 1.22 eV, with the lowest optical bandgaps occurring in those with metal-precursor absorber processes. Devices with Zn(O, S) or thin CdS buffers had quantum efficiencies above 90% down to 400 nm. Most voltages were 250–300 mV below the Shockley–Queisser limit for their bandgap. Electroluminescence intensity tracked well with the respective voltage deficits. Fill factor (FF) was as high as 95% of the maximum for each device's respective current and voltage, with higher FF corresponding to lower diode quality factors (∼1.3). An in-depth analysis of FF losses determined that diode quality reflected in the quality factor, voltage-dependent photocurrent, and, to a lesser extent, the parasitic resistances are the limiting factors. Different absorber processes and device structures led to a range of electrical and physical characteristics, yet this investigation showed that multiple fabrication pathways could lead to high-quality and high-efficiency solar cells.**

***Index Terms*—Auger electron spectroscopy (AES), capacitance, characterization, correlation, Cu(In, Ga)Se_2 (CIGS), internal quantum efficiency (IQE), thin-film photovoltaics.**

I. Introduction

COPPER indium gallium diselenide (CIGS) photovoltaics are some of the most efficient thin-film solar cells available. Although CIGS record-cell efficiencies have increased steadily over time, there is room for improvement because the theoretical efficiency limit of 29% [1] has not been reached. A large gap also exists between the efficiencies of small-area prototype cells and the efficiencies of commercially available modules. For example, the current world record CIGS cell efficiency is 22.6%, whereas the most module products have efficiencies in the 13–15% efficiency range.

To address the cell-to-module gap in CIGS, our team is a part of the Foundational Program to Advance Cell Efficiency, sponsored by the U.S. Department of Energy and the National Science Foundation. The team consists of the National Renewable Energy Laboratory, universities, and industrial partners. Under this program, we have a unique opportunity to work with the CIGS industry to solve company-specific problems. With the diverse expertise of participating organizations, the team offers assistance so that the industrial partners can increase the efficiency of their products.

High-efficiency CIGS-based devices can be made from many different manufacturing techniques. In fact, world record CIGS solar cells over the past few years have been made by three different processes. The current world record from Zentrum für Sonnenenergie- und Wasserstoff-Forschung Baden-Wüttemberg (ZSW) stands at 22.6%, and the cell was made by a three-stage process [2]. The previous record cell from Solar Frontier, having 22.3% efficiency, was made from a metal precursor with a subsequent selenization and sulfurization process [3]. In 2013, the efficiency record of 20.4% was set by EMPA, who used a low-temperature CIGS process on a polyimide substrate [4]. Note that the processing differences were in the CIGS absorber. Many additional modifications in device structure are possible, and together, they determine the final solar cell efficiency.

The purpose of this study was to characterize devices from multiple solar cell fabricators to gain insight into their similarities and differences. A host of measurement techniques was employed and will be described below. Losses were quantified to show how each device's performance departed from an ideal device. Through this investigation, we sought to learn from comparisons between device structures and absorber processes, and to approach tangible solutions for closing efficiency gaps between lab cells and large-scale manufacturing.

II. Experiment

A. Cell Structures and Fabrication

Samples were selected from six different solar cell fabricators consisting of research laboratories and industrial partners. These samples were not intended to represent champion solar cells from each fabricator but, instead, to represent an average device performance that would be expected from each fabrication process. Each cell fabricator submitted six nominally identical samples that had between four and seven small-area devices per sample ($0.4-1.0$ cm^2). Measurement data presented

Manuscript received September 16, 2016; accepted October 3, 2016. Date of publication November 3, 2016; date of current version December 20, 2016. This work was supported by the U.S. Department of Energy under Contract DE-AC36-08GO28308 with the National Renewable Energy Laboratory. The U.S. Government retains and the publisher, by accepting the article for publication, acknowledges that the U.S. Government retains a nonexclusive, paid up, irrevocable, worldwide license to publish or reproduce the published form of this work, or allow others to do so, for U.S. Government purposes.

L. M. Mansfield and R. L. Garris are with the National Renewable Energy Laboratory, Golden, CO 80401 USA (e-mail: Lorelle.Mansfield@nrel.gov; Rebekah.Garris@nrel.gov).

K. D. Counts and J. R. Sites are with the Department of Physics, Colorado State University, Fort Collins, CO 80523 USA (e-mail: countskahl@gmail.com; james.sites@colostate.edu).

C. P. Thompson and W. N. Shafarman are with the Institute of Energy Conversion, University of Delaware, Newark, DE 19716 USA (e-mail: cpt@udel.edu; wns@udel.edu).

K. Ramanathan was with the National Renewable Energy Laboratory, Golden, CO 80401 USA. He is now at Stion Corporation, San Jose, CA 95110 USA (e-mail: kramanathan@stion.com).

Color versions of one or more of the figures in this paper are available online at http://ieeexplore.ieee.org.

Digital Object Identifier 10.1109/JPHOTOV.2016.2616188

2156-3381 © 2016 IEEE. Personal use is permitted, but republication/redistribution requires IEEE permission.
See http://www.ieee.org/publications_standards/publications/rights/index.html for more information.

TABLE I
SUMMARY OF CELL STRUCTURES AND FABRICATION PROCESSES FOR SIX DIFFERENT FABRICATORS

Fabricator	Substrate	Absorber Process	Absorber	Buffer	Cell Structure
A	Glass	Three-stage Coevaporation	$Cu(In, Ga)Se_2$	CdS	ZnO:Al/i-ZnO/CdS/CIGS/Mo
B	Glass	Three-stage Coevaporation	$(Ag, Cu)(In, Ga)Se_2$	CdS	ITO/i-ZnO/CdS/ACIGS/Mo
C	Stainless steel (R2R)	Cosputtering	$Cu(In, Ga)Se_2$	CdS	ZnO:Al/i-ZnO/CdS/CIGS/Mo
D	Stainless steel (R2R)	Three-stage Coevaporation	$Cu(In, Ga)Se_2$	CdS	ITO/i-ZnO/CdS/CIGS/Mo
E	Glass	Metal-precursor reaction with H_2 Se/H_2 S	$Cu(In, Ga)(S,Se)_2$	Thin CdS	ZnO:B/ZnO/CdS/CIGSSe/Mo
F	Glass	Metal-precursor reaction with H_2 Se/H_2 S	$Cu(In, Ga)(S,Se)_2$	Thin Zn(O, S)	ZnO:B/ZnO/Zn(O, S)/CIGSSe/Mo

in the next sections were taken from either finished devices or bare absorbers. (A bare absorber was obtained from a finished device by etching back the metallic grid, transparent conducting oxide (TCO), and buffer in dilute HCl.) Samples from each of the six fabricators will be identified herein by the letters A–F in this study, and will be referred to as CIGS, even though sample B is ACIGS and samples E and F are CIGSSe. Device finishing was completed by each fabricator such that finished CIGS devices in this study have varying absorber, buffer, and TCO processes. This means that samples have different amounts of surface reflection, window and buffer layer absorption, and TCO resistance. In general, antireflection coatings were applied. Processing information is summarized in Table I.

An overarching goal in comparing aspects of all six samples was to reveal some of the biggest common denominators that drive efficiency in CIGS technology. Toward accomplishing this, some interesting opportunities immediately presented themselves, based on processing information alone. Samples E and F were made with a similar absorber process, but with different buffer layers. Samples A, B, and D were deposited by three-stage coevaporation, although sample B used Ag in the absorber and sample D used a stainless-steel substrate. Samples C and D were both deposited on stainless-steel substrates, although they had different absorber processes. Despite these fabrication variations, all of these processes can demonstrate high-efficiency devices.

B. Scanning Electron Microscopy

Scanning electron microscopy (SEM) images were collected on absorber cross sections to get information about the film morphology. The images shown in Fig. 1 are of representative samples from each cell fabricator. The average thickness shown on each image was calculated from several measurements collected on the same sample. Each image is displayed on the same size scale, with window dimensions being 2.2 μm wide and 4.5 μm high.

Comparing all six SEM images reveals interesting topographical features that result from the varying absorber processes. The absorbers deposited by coevaporation (samples A, B, and D) and cosputtering (sample C) show large grain structure and clean interfaces between the absorber and the Mo. The sulfur containing absorbers (samples E and F) show smaller grains and have voids at the interface between the absorber and the Mo.

C. Auger Emission Profiling

Auger electron spectroscopy (AES) measurements were collected on bare absorbers from each cell fabricator. Depth profiles

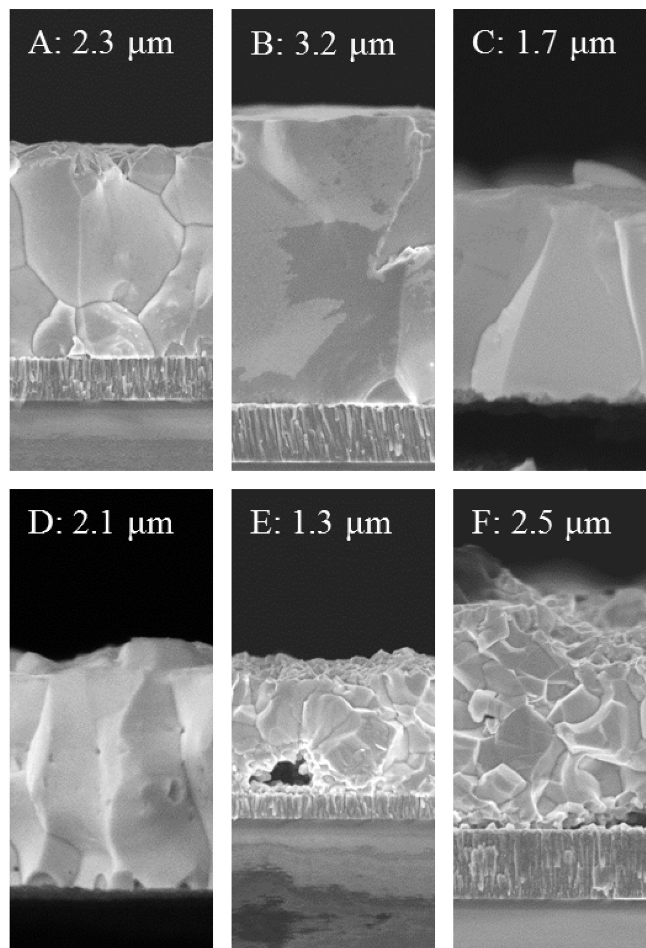

Fig. 1. SEM images on representative absorbers in samples A–F, as annotated on each image. Note that all images are shown on the same size scale, and the average absorber thickness measured from each image is as indicated in the annotations.

of Cu, In, Ga, Se, S, and Mo were measured with a 5-kV, 20-nA primary electron beam over a 400-μm^2 area of each sample. Data were collected with the sample surface tilted at 30° from the electron beam and analyzer. The rate of sputter profiling and the calculation of sensitivity factors are detailed in [5]. The endpoints of each sputter profile were determined by Mo concentration. There is no AES profile for sample B because its high resistivity caused a large amount of charging during the measurements, which prevented useful data from being obtained.

The AES composition measurements were used to calculate bandgap profiles. First, we obtained the gallium ratio $X = \mathrm{Ga}/(\mathrm{In} + \mathrm{Ga})$, as well as the sulfur ratio $Y = \mathrm{S}/(\mathrm{S} + \mathrm{Se})$.

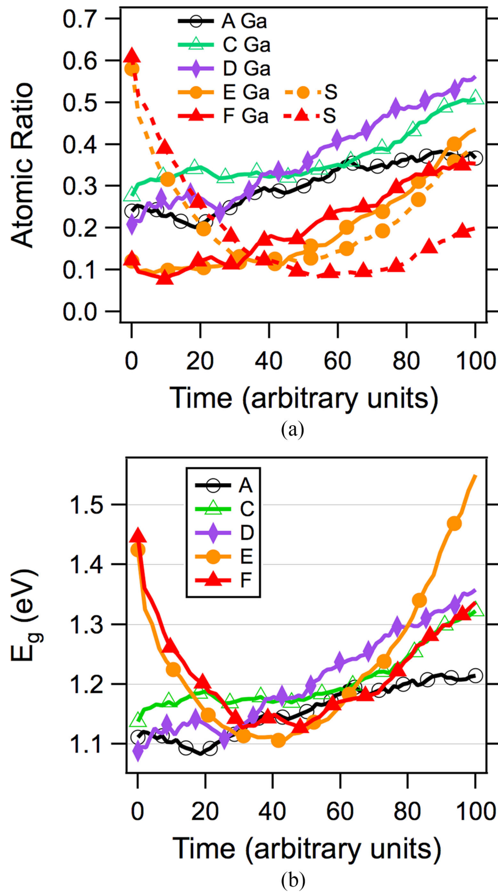

Fig. 2. (a) Atomic ratios calculated from AES. Solid lines represent the ratio of $X = \mathrm{Ga}/(\mathrm{In} + \mathrm{Ga})$, and dashed lines represent the ratio of $Y = \mathrm{S}/(\mathrm{Se} + \mathrm{S})$. (b) Bandgap profiles calculated from (1) for representative absorbers from samples A and C–F. Sputter time for each profile has been normalized to 100; actual sputter times varied from 96 to 164 min. Sample B is not included due to its high resistivity.

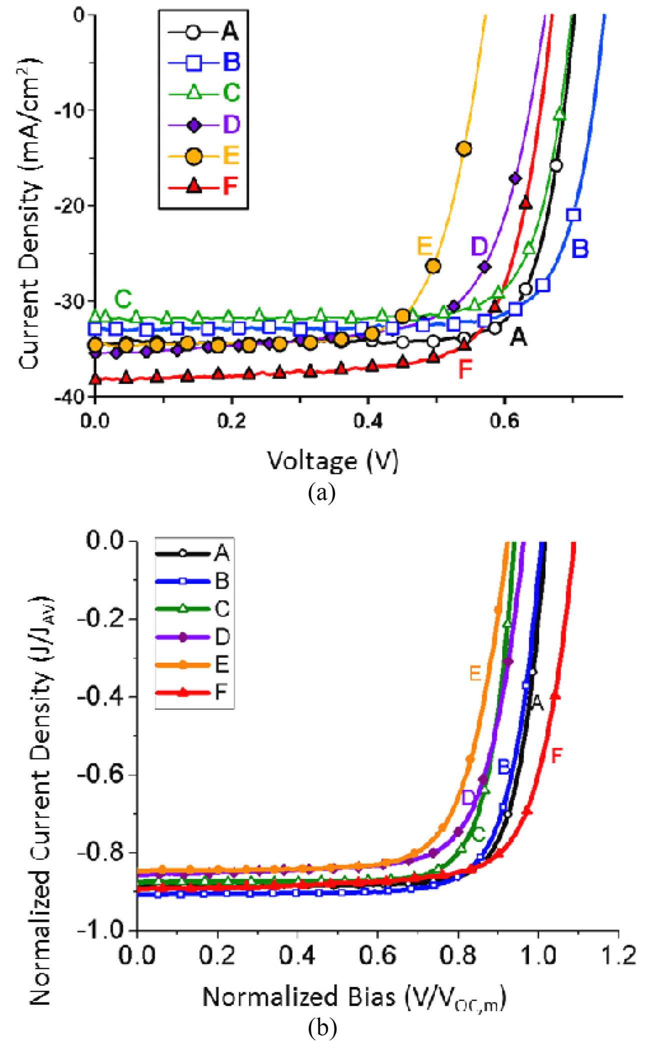

Fig. 3. (a) *J–V* curves and (b) normalized *J–V* curves of representative CIGS devices.

The atomic ratios of the Ga (X, solid lines) and S (Y, dashed lines) are shown in Fig. 2(a). These were then used to calculate AES bandgap $(E_{g,\mathrm{AES}})$ in electronvolts according to, and copied from [6]:

$$E_{g,\mathrm{AES}}(X,Y) = 1.00 + 0.13X^2 + 0.08X^2Y + 0.13XY + 0.55X + 0.54Y. \quad (1)$$

The variation in smoothed bandgap profiles in Fig. 2(b) demonstrates the large bandgap range of CIGS absorbers that can lead to high-efficiency solar cells.

The bandgap gradients in samples without sulfur mirror the gradients in the gallium ratios, whereas the samples with sulfur are due to the gradients in both the gallium ratio and the sulfur ratio. Sample A showed a notch structure in the bandgap profile. Sample C had a graded bandgap that was lowest at the front and steeply increased toward the back. Sample D showed a nearly uniform bandgap gradient that increased steadily from front to back. The U-shape of the sulfur ratio and the increasing gallium ratio at the back created a strong U-shape in the bandgap profile of sample E. The high sulfur ratio at the front and the high gallium ratio at the back are combined to make a lopsided U-shape bandgap profile in sample F.

D. Electrical Characterization of Finished Devices

Comparative measurements [current–voltage, internal quantum efficiency (IQE), capacitance, electroluminescence (EL), and light-beam-induced current (LBIC)] were made on at least two devices from each of the cell fabricators. There was little difference in electrical measurements among devices from the same lab, which indicates a high level of reproducibility and uniformity in each fabrication process. Comparisons between representative devices from each fabricator were used to understand how the different absorber processes and device structures affect overall electrical performance.

1) Current–Voltage Analysis: Current density versus voltage (*J–V*) data were obtained using four-point probe measurements. Devices were measured at 25 °C under a 100 mW/cm^2 light intensity produced by a class A solar simulator. Light (J) and dark (J_D) *J–V* curves were measured for every device, with ~5-mV steps in applied voltage.

TABLE II
PARAMETER TABLE FROM J–V CURVES OF REPRESENTATIVE DEVICES

Sample	$V_{\rm OC}$ (mV)	$J_{\rm SC}$ (mA/cm^2)	FF (%)	η (%)	R_S ($\Omega\cdot$cm^2)	R_{Sh} ($\Omega\cdot$cm^2)	A	J_0 (mA/cm^2)	IQE E_g (eV)
A	701	34.3	80.7	19.4	0.3	10 000	1.3	2.5e–8	1.17
B	742	33.0	77.8	19.1	0.4	5000	1.6	2.9e–7	1.22
C	698	32.3	77.4	17.5	0.2	6000	1.6	1.3e–6	1.22
D	656	34.3	69.3	15.6	0.5	250	1.8	1.8e–5	1.18
E	571	34.6	72.3	14.3	0.8	2500	1.5	1.1e–5	1.09
F	669	38.3	73.2	18.8	0.4	1100	1.7	7.5e–6	1.05

In addition to extracting open-circuit voltage $(V_{\rm OC})$, short-circuit current density $(J_{\rm SC})$, fill factor (FF), and efficiency (η), a single-diode model, for which the current can be written as

$$J(V) = J_0 \exp\left[\frac{q(V - R_S J)}{AkT}\right] + \frac{V}{R_{\rm Sh}} - J_L(V) \qquad (2)$$

was used to determine series resistance (R_S), shunt resistance $(R_{\rm Sh})$, diode ideality factor (A), diode saturation current density (J_0), and voltage-dependent photocurrent $(J_L(V))$ [7].

The J–V curves for one representative device from each cell fabricator are shown in Fig. 3(a), with the key J–V and diode parameters given in Table II. All of the devices had respectable efficiencies, with no obvious distortions in their J–V curves. A significant spread in the effective bandgaps among the devices led to the typical tradeoff between current and voltage. The highest $V_{\rm OC}$ device, i.e., sample B, represents the highest bandgap in this study, whereas the highest $J_{\rm SC}$ device, i.e., sample F, has the lowest effective bandgap. The highest FF device, i.e., sample A, corresponds to the lowest diode ideality factor A.

The current densities of all the devices corresponded to a collection of 80–85% of the photons above the bandgap. Most of the voltages were 250–300 mV below the Shockley–Queisser limit for the device's bandgap, which is typical of CIGS cells, although cell B was only 170 mV less. The values of FF were generally good, that is, as high as 95% of the maximum for the cells' respective currents and voltages, with higher FF corresponding to lower values of the diode ideality factor A. The impacts of R_S and $R_{\rm Sh}$ on FF were generally small. Losses in J–V, and specifically in FF, will be further explored in Section III.

2) Internal Quantum Efficiency: The external quantum efficiency (EQE) and reflection of each device were measured in parallel. Following the adjustment for reflectance, the IQE curves for six representative devices are shown in Fig. 4. The estimated bandgaps are marked with symbols. For cells E and F, the long-wavelength cutoff was out of instrumental range, and the bandgap was estimated based on the shift from the other curves. The bandgaps derived from IQE are included in Table II. Measurements were performed by illuminating each sample with a monochromatic beam with a full-width half-maximum of ~10 nm. The accuracy of the irradiance spectrum was verified using a calibrated Si solar cell.

The optical bandgap E_g was determined from IQE by finding the local minimum in dIQE / $d\lambda$, which yields $E_g + E_U/2$ [8], where λ is the wavelength corresponding to the bandgap, and E_U is the Urbach energy. Because E_U is typically 10–30 meV for CIGS [9], this dIQE / $d\lambda$ method gives a good estimation of E_g.

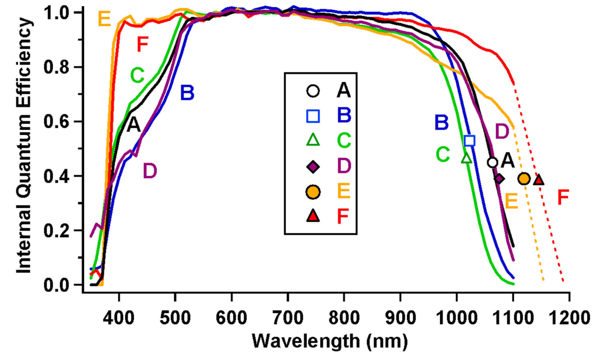

Fig. 4. IQE curves of representative CIGS devices.

The IQE data were measured using a step size of $\Delta\lambda = 10$ nm, and the local minimum of dIQE / $d\lambda$ was determined using a quadratic fit.

All of the IQE curves approach 100% over a broad part of the solar spectrum. The devices with little or no CdS (samples E and F) had IQE above 90% down to 400 nm. Those devices were also made with sulfur and showed more gradual IQE cutoffs in the longer wavelengths approaching their bandgaps, affirming that they have significantly graded bandgaps, as previously demonstrated by AES.

3) Capacitance–Voltage Analysis: Capacitance versus voltage (C–V) measurements were collected with an LCR meter in the parallel capacitance mode. Voltage modulation was 20 mV, and the ac voltage signal was 50 kHz. Conductance was tracked during measurement, and only data with a phase angle near 90° are included. Fig. 5 shows the absorber carrier density $(N_{\rm CV})$ calculated from C–V curves for a representative device from each cell fabricator. The symbol on each curve is the zero-voltage point with reverse bias to the right and forward bias to the left. For each cell, the capacitance was first measured as a function of frequency to check for possible dispersion. For five of the cells, $N_{\rm CV}$ was in the mid-10^{15} to high-10^{16} cm^{-3} range, with corresponding depletion widths W of 0.3–0.4 μm. The device from sample B, however, had a much lower $N_{\rm CV}$ near 10^{15} cm^{-3} and a higher W near 1 μm.

4) Cell Uniformity: The uniformity of the cells was examined by EL and LBIC. The EL images in Fig. 6(a) are reasonably uniform, although various types of nonuniformities can be seen, especially in one of the devices (sample D) that had a stainless-steel substrate. EL intensity is sensitive to a variety of nonuniformities, and it is common to see features in the images even for the best devices. The placement of the contact and the

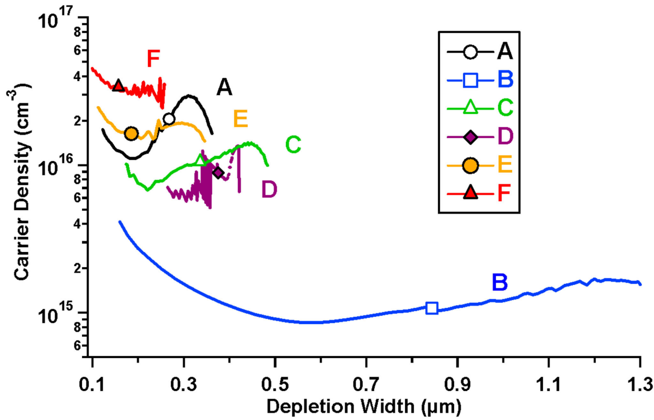

Fig. 5. Absorber carrier density (N_{CV}) versus depletion width *W* calculated from *C–V* measurements.

grid patterns are seen clearly on each of the images. The logarithm of each intensity magnitude is tracked with the V_{OC} of each device [see Fig. 6(b)], as expected [10] [note that various intensity scales are used in Fig. 6(a)]. One thing of note, which is most clearly exemplified in the EL image of sample B, is that there is a voltage drop with distance away from the contact, and hence, the EL emission is brighter closer to the grid fingers.

LBIC maps [11] of each cell [see Fig. 6(c)] show the relative photoresponse as a function of position over the cell area. The LBIC maps also show the grid patterns and contact area clearly, but they are less sensitive to scratches and other defects than the EL images. They do show occasional defects, but because these defects are well localized, one can reasonably conclude that they have only a minor effect on cell performance.

III. *J–V* Loss Analysis and Discussion

An in-depth analysis was performed on *J–V* losses, with particular focus on mechanisms causing losses in FF. For these already high-efficiency devices, further improvements in performance can be difficult to attain. This analysis seeks to reveal areas of device performance in which improvements may lead to enhancement of device efficiency.

A. Fill Factor Loss Analysis

A quantitative loss analysis of FF was performed assuming the single-diode model in (2). We correct the measured *J–V* data for R_{Sh} losses by removing the current contribution from the shunt resistance to determine J', where

$$J' = J - \frac{V}{R_{\mathrm{Sh}}}. \quad (3)$$

Similarly, $V' = V - R_S J$ so that $J'(V')$ is the measured *J–V* data corrected for both series and shunt resistances.

Because we are assuming superposition, i.e., $J'(V') = J'_D(V') - J_L(V')$, we can quantify the effect of voltage-dependent collection [12]. The difference between dark and light *J–V* curves is used to calculate a collection function $\eta_C(V')$ so that $J_L(V') = J_{L0}\,\eta_C(V')$. Here, J_{L0} is the optically limited current [12].

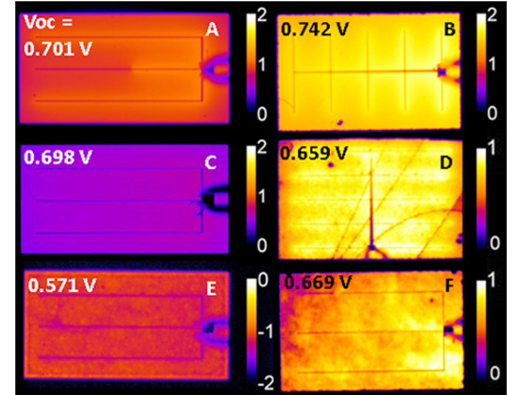

(a)

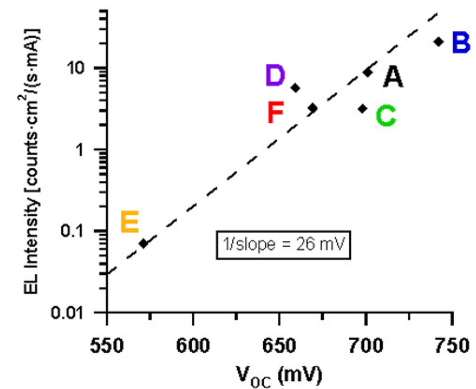

(b)

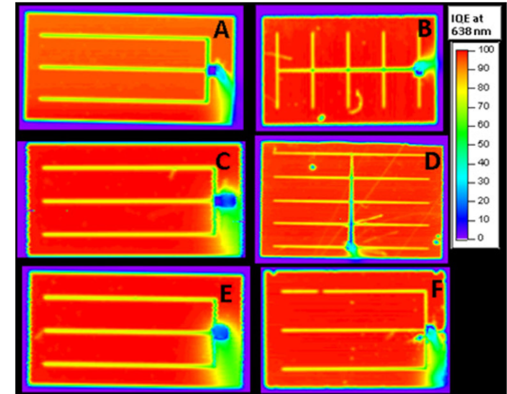

(c)

Fig. 6. (a) EL images of representative cells, (b) variation of EL intensity with open-circuit voltage, and (c) LBIC images of the same six cells.

The losses in FF due to shunting, series resistance, and voltage-dependent current collection can be quantified incrementally. FF$'$ is defined as the value of FF corrected for shunt losses, which is determined from a plot of $J'(V)$ versus *V*. The value of FF corrected for both shunt and series losses is FF$''$ and is determined from $J'(V')$ versus V'. Including all three loss mechanisms, FF$''_{\mathrm{C}}$ is determined from $J'_C(V')$ versus V', where $J'_C(V') = J'_D(V') - J_{L0}$, and $J'_D(V')$ is $J_D(V)$ corrected for both series and shunt resistance. Fig. 7 shows *J–V* curves of sample F corrected for R_{Sh}, R_S, and $J_L(V)$ effects.

It should be noted that FF loss attributed to voltage-dependent current collection could also be caused by irradiance-dependent

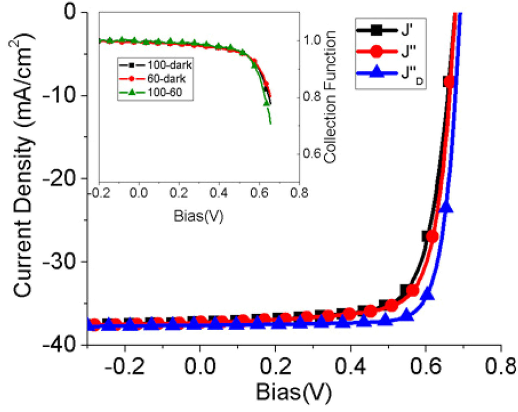

Fig. 7. *J–V* curves corrected for R_S, $R_{\rm Sh}$, and $J_{\rm L}(V)$ losses, as well as the collection function (inset) calculated at different intensities, for sample F.

TABLE III
PARAMETER TABLE FROM NORMALIZED *J–V* CURVES FOR REPRESENTATIVE DEVICES

Sample	$V_{OC}/V_{OC,m}$ (%)	$E_g - V_{OC}/q$ (meV)	J_{SC}/J_{AV} (%)	FF/ FF$_m$ (%)	η/η_m (%)
A	102	460	89	96	89
B	101	470	91	92	86
C	94	520	88	94	79
D	96	500	86	89	75
E	92	520	85	89	73
F	109	410	89	92	93

recombination (i.e., changes in *A* and J_0 with illumination intensity). Using a procedure described in [12], and inset in Fig. 7 (for sample F, for example), *J–V* curves measured at three different irradiances (0, 60, 100 mW/cm^2) were used to verify that the collection function was independent of incident light intensity. Thus, the additional loss between FF$''$ and FF$''_C$ is likely due to current collection.

B. Normalization of J–V Parameters With Bandgap

To compare the devices, their *J–V* parameters were normalized with respect to bandgap. Expected $V_{\rm OC}$, FF, $J_{\rm SC}$, and η for each bandgap were determined using an empirical single-diode model with no parasitic resistive losses. J_0 was calculated by $J_0 = \chi n_i$, where $n_{\rm i}$ is the intrinsic carrier density, which varies with $\exp(-E_g)$, and χ represents a fixed recombination term. In this case, χ was set so that at $E_g = 1.15$ eV, the model device would have $\eta = 22\%$, FF $= 82\%$ $V_{\rm OC} = 701$ mV, and $J_{\rm SC} = 40.3$ mA/ cm^2 determined by the available current ($J_{\rm AV}$) in the AM1.5g spectrum. For each device in the sample set, parameters were normalized by the predicted model performance, represented as $V_{\rm OC}/V_{{\rm OC},m}$, $J_{\rm SC}/J_{\rm AV}$, FF/FF$_m$, and η/η_m, where the subscript *m* refers to the model parameter for the bandgap of that device. Normalized *J–V* curves for a representative device from each fabricator are shown in Fig. 3(b), and the relative *J–V* parameter losses are listed in Table III. Based on the 10-nm wavelength step size for the EQE measurements (not shown), we estimate a rough uncertainty in E_g of 10 nm.

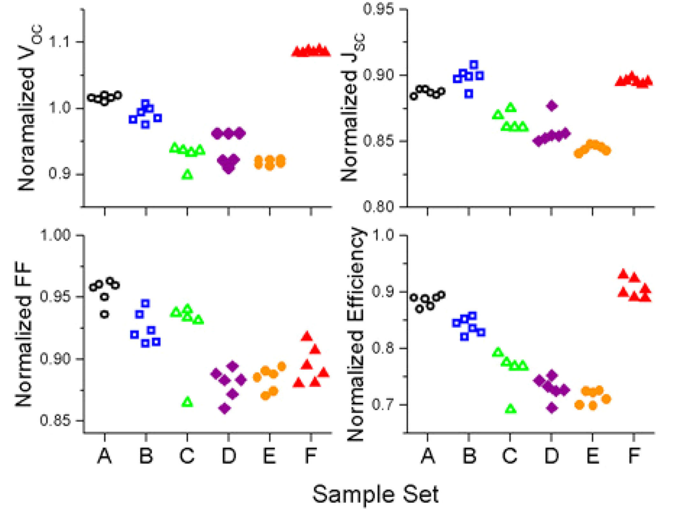

Fig. 8. Normalized *J–V* parameters. Multiple symbols represent separate devices per substrate. $V_{\rm OC}$ was normalized by $V_{{\rm OC},{\rm m}}$, $J_{\rm SC}$ was normalized with $J_{\rm AV}$, FF was normalized with FF$_m$, and η was normalized with η_m.

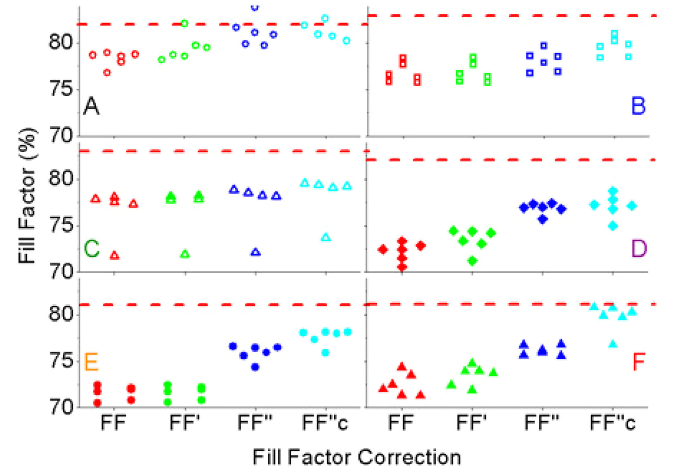

Fig. 9. FF loss analysis, where the red dashed lines (FF$_m$) represent the extracted FF at that device's bandgap, based on an analytical model. Note the general increase in FF from FF to FF$''_C$.

This would give error bars of $\pm1.2\%$ for $V_{\rm OC}/V_{{\rm OC},m}$, $\pm1\%$ for $J_{\rm SC}/J_{\rm AV}$, $\pm0.25\%$ for FF/FF$_m$, and $\pm0.5\%$ for η/η_m. Normalized *J–V* parameters for all devices are shown in Fig. 8. Values of FF, FF$'$, FF$''$, and FF$''_C$ are shown in Fig. 9, relative to FF$_m$.

The device with highest normalized efficiency was from an industrial process (sample F), and was followed closely by two laboratory-scale processes (samples A and B). The three other devices C, D, and E are all from commercial processes and have larger deficits in $V_{\rm OC}/V_{{\rm OC},m}$ and $J_{\rm SC}/J_{\rm AV}$. Sample C had high FF/FF$_m$, similar to the best devices. There is no strong correlation between substrate and normalized efficiency, although devices on stainless-steel substrates appear to have a lower $V_{\rm OC}/V_{{\rm OC},m}$ that could be a result of iron contamination [13].

Bandgap gradients can explain some variation in $V_{\rm OC}/V_{{\rm OC},m}$. Samples with bandgap gradients were A, B, E,

TABLE IV
FILL FACTOR LOSS BREAKDOWN FOR SIGNIFICANT LOSSES (>2%) BY SAMPLE SET

FF Loss Mechanism	Samples
Series resistance, R_S	D, E, and F
Voltage-dependent photocurrent, $J_L(V)$	B, E, and F
Diode parameters, A and J_0	B, C, D, and E

and F. For this discussion, the bandgap profile for sample B is based on the secondary-ion mass spectrometry profile provided in [14], which was measured on a nominally identical device. Samples A and B have relatively small front bandgap gradients, whereas samples E and F have higher front bandgap gradients due to sulfur incorporation. Most of the samples with front bandgap gradients had a high ratio of $V_{\rm OC} / V_{{\rm OC},m}$. When samples E and F were compared, variation in $N_{\rm CV}$ (see Fig. 5) only accounted for a small variation in $V_{\rm OC}$. Either a higher bulk or interface recombination rate could be responsible for increased J_0 and reduced $V_{\rm OC}$, despite similar bandgap profiles [see Fig. 2(b)]. Samples A, B, and F exhibit some of the limitations that arise when defining optical bandgap in samples where AES bandgap varies widely with thickness. These samples have $V_{\rm OC} / V_{{\rm OC},m} \geq 1$, suggesting that the bandgap that limits recombination can be decoupled from the optical bandgap that limits $J_{\rm SC}$. Since $V_{OC,m}$ is a function of the E_g from EQE, which is related to the minimum E_g, a front bandgap gradient can provide a larger than expected $V_{\rm OC}$, without compromising $J_{\rm SC}$. Numerical modeling and measurements on samples similar to sample B have shown that this is plausible [13], [14].

Variations in $J_{\rm SC} / J_{\rm AV}$ can be explained by several factors. Comparing samples E and F, the steeper back bandgap gradient resulted in a "softer" IQE shoulder at long wavelengths, which reduced $J_{\rm SC}$. Comparing devices B and C, which also had similar E_g, device B had a higher long-wavelength response and sharper shoulder. This could be due to a higher minority-carrier lifetime, or the wide depletion width in sample B allowing for field-assisted collection. Sample F had the highest ratio of $J_{\rm SC} / J_{\rm AV}$ due to the high bandgap of the Zn(O, S) buffer layer, as well as higher long-wavelength response. The high long-wavelength response is indicative of a longer minority-carrier lifetime, and is in good agreement with higher $V_{\rm OC} / V_{{\rm OC},m}$.

C. Fill Factor Loss Mechanisms

Looking further at FF losses, FF $\approx$ FF$'$ in Fig. 9 indicates that shunting was not a major loss in most of the devices. Thus, the three dominant FF loss mechanisms were series resistance, voltage-dependent current collection, and recombination (or high A). The latter loss mechanism is determined relative to the expected FF from the empirical model. The samples that had losses $> 2\%$ for each of these mechanisms are listed in Table IV.

Several of the devices suffered from R_S losses $> 2\%$. Samples E and F were optimized for monolithic integration, therefore their back-electrode sheet resistances were probably not optimized for small cells with grids. Often, industrial process parameters are optimized for modules or large-area cells, therefore R_S losses in nonoptimized small cells are not of major consequence.

The FF losses due to $J_L(V)$ and recombination are related to the performance of the p-n junction and are of more interest than R_S losses. Significant $J_L(V)$ losses are seen in samples B, E, and F. Of these, samples E and F have front bandgap gradients that may reduce FF [16]. Sample B has a lower $N_{\rm CV}$ compared with the other samples, which can result in a weaker electric field in the depletion region. If drift time across the field region is longer than minority-carrier lifetime, a loss in $J_L(V)$ can result [12]. Low minority-carrier lifetime can also result in reduced $J_L(V)$. The effects of low minority-carrier lifetime are evident in long-wavelength IQE, as well as low FF. In sample E, a "soft" IQE shoulder at long wavelengths (see Fig. 4), and lower ratios of $V_{\rm OC} / V_{{\rm OC},m}$ and η / η_m, suggest high recombination losses that may be an effect of low minority-carrier lifetimes.

For significant FF loss due to A and J_0, there is a gap between FF$''_C$ and FF$_m$ (dashed line), as is apparent in Fig. 9 for samples B, C, D, and E. It is worthwhile to look at samples A and F, which did not have significant recombination losses (FF$''_C \approx$ FF$_m$). The processes used to grow films A and F were radically different from each other, which demonstrates that there are multiple pathways to high-quality absorber materials that have low recombination losses. However, the $J_L(V)$ losses in low-recombination samples affirm that bandgap grading is critical toward optimizing device performance. This has been demonstrated using numerical modeling, which showed strong correlations between bandgap profiles and $V_{\rm OC}$ [15] and between bandgap gradients and FF losses [16].

IV. CONCLUSION

High-quality CIGS solar cells were fabricated at six laboratories with several different compositions, structures, and deposition techniques. Despite significant variations in the CIGS bandgaps, bandgap profiles, carrier densities, and morphology, the device performance of the six sets of cells was similar. The voltages were generally high as compared with the maximum 1 sun value for the respective absorber bandgaps. The diode ideality factors ranged between 1.3 and 1.8 and were a significant limitation to the FF, which varied from 80% for the smallest value down to about 70% for the largest. The voltage dependence of collection, however, also played a role, particularly for the cells with the smallest bandgap. In general, the parasitic series and shunt resistances were lesser factors in limiting the FF. The IQEs of all the cells were close to unity over a broad spectral range, and the photocurrents, as expected, reflected the CIGS bandgap cutoffs and the short-wavelength transparency of the buffers. The CIGS carrier densities were in the low 10^{16} cm^{-3} range, except for the Ag-containing cells which were a decade lower. Cell uniformity as determined by EL and LBIC was gen-

erally good, and although there were isolated features seen, these were not a significant factor limiting cell performance.

ACKNOWLEDGMENT

The authors would like to thank J. W. Pankow for AES, B. To for SEM, K. Bowers and C. Beall for device finishing, and R. Geisthardt for advice on device measurements.

REFERENCES

[1] W. Shockley, "Detailed balance limit of efficiency of p-n junction solar cells," *J. Appl. Phys.*, vol. 32, no. 3, pp. 510–519, 1961.

[2] P. Jackson *et al.*, "Effects of heavy alkali elements in Cu(In, Ga)Se_2 solar cells with efficiencies up to 22.6%," *Phys. Status Solidi RRL*, vol. 10, pp. 583–586, 2016.

[3] "Solar frontier achieves world record thin-film solar cell efficiency: 22.3%," Dec. 8, 2015. [Online]. Available: http://www.solar-frontier.com/eng/news/2015/C051171.html.P

[4] A. Chirilă, "Potassium-Induced surface modification of Cu(In, Ga)Se_2 thin films for high-efficiency solar cells," *Nature Mater.*, vol. 12, no. 12, pp. 1107–1111, 2013.

[5] C. L. Perkins, B. Egaas, I. Repins, and B. To, "Quantitative analysis of graded $Cu(In_{1-x},Ga_x)Se_2$ thin films by AES, ICP-OES, and EPMA," *Appl. Surf. Sci.*, vol. 257, pp. 878–886, 2010.

[6] M. Bar *et al.*, "Determination of the band gap profile of the penternary $Cu(In_{1-X}Ga_X)(S_YSe_{1-Y})_2$ chalcopyrite from its composition gradient," *J. Appl. Phys.*, vol. 96, no. 7, pp. 3857–3860, 2004.

[7] S. Hegedus and W. Shafarman, "Thin-Film solar cells: device measurements and analysis," *Prog. Photovolt., Res. Appl.*, vol. 12, pp. 155–176, 2004.

[8] C. J. Hages, N. J. Carter, and R. Agrawal, "Generalized quantum efficiency analysis for Non-Ideal solar Cells: Case of $Cu_2ZnSnSe_4$," *J. Appl. Phys.*, vol. 119, 2016, Art. no. 014505.

[9] J. T. Heath, J. D. Cohen, W. N. Shafarman, D. X. Liao, and A. A. Rockett, "Effect of Ga content on defect states in $CuIn_{1-x}Ga_xSe_2$ photovoltaic devices," *Appl. Phys. Lett.*, vol. 80, 2002, Art. no. 4540.

[10] J. M. Raguse and J. R. Sites, "Correlation of electroluminescence with Open-Circuit voltage from CdTe solar cells," *J. Photovolt.*, vol. 5, pp. 1175–1178, 2015.

[11] R. M. Geisthardt and J. R. Sites, "Nonuniformity characterization of CdTe solar cells using LBIC," *J. Photovolt.*, vol. 4, pp. 1114–1118, 2014.

[12] S. Hegedus, D. Desai, and C. Thompson, "Voltage dependent photocurrent collection in CdTe/CdS solar cells," *Prog. Photovolt., Res. Appl.*, vol. 15, pp. 587–602, 2007.

[13] T. Eisenbarth, R. Caballero, C. A. Kaufmann, A. Eicke, and T. Unold, "Influence of iron on defect concentrations and device performance for Cu(In, Ga)Se_2 Solar Cells on stainless steel substrates," *Prog. Photovolt., Res. Appl.*, vol. 20, no. 5, pp. 568–574, 2012.

[14] C. P. Thompson, L. Chen, W. N. Shafarman, and J. Lee, "Bandgap Gradients in (Ag, Cu)(In, Ga)Se_2 thin film solar cells deposited by three-stage co-evaporation," in *Proc. IEEE Photovolt. Spec. Conf.*, New Orleans, LA, USA, pp. 1–6, 2015.

[15] I. L. Repins *et al.*, "Comparison of device performance and measured transport parameters in widely-varying Cu(In, Ga)(Se,S) solar cells," *Prog. Photovolt., Res. Appl.*, vol. 14, pp. 25–43, 2006.

[16] C. P. Thompson, D. Lee, and W. N. Shafarman, "Characterization and numerical modeling of Cu(In, Ga)$(S,Se)_2$ solar cells," in *Proc.42nd IEEE Photovolt. Spec. Conf.*, New Orleans, LA, USA, pp. 1–6, 2015.

Authors' photographs and biographies not available at the time of publication.